Spin spirals in underdoped $La_{2-x}Sr_xCuO_4$ and $YBa_2Cu_3O_{6+y}$: Differences and similarities

O. P. Sushkov
School of Physics, University of New South Wales, Sydney 2052, Australia
(Received 10 January 2009; revised manuscript received 5 March 2009; published 13 May 2009)

Contrary to a widely accepted view the phase diagrams of $La_{2-x}Sr_xCuO_4$ (LSCO) and $YBa_2Cu_3O_{6+y}$ (YBCO), in spite of similarities are remarkably different. Both the electric conduction properties and the commensurate/incommensurate spin ordering properties differ dramatically. It is argued that the role of disorder in YBCO is insignificant while the bilayer structure is crucial. On the other hand in LSCO the intrinsic disorder to a large extent drives the properties of the system. The developed approach explains the low-temperature magnetic properties of the systems. The most important point is the difference with respect to the incommensurate spin ordering, including the difference in the incommensurate pitches. The understanding of mechanisms for the differences provides a deep insight into generic physics of the systems.

DOI: 10.1103/PhysRevB.79.174519 PACS number(s): 74.72.−h, 75.25.+z, 75.30.Fv, 78.70.Nx

I. INTRODUCTION

In early days of high-temperature superconductivity there was a belief that the phase diagram of $La_{2-x}Sr_xCuO_4$ (LSCO) represents a generic phase diagram of cuprate superconductors. Nowadays it has become clear that, in spite of similarities, there are very important differences between different cuprates. LSCO and $YBa_2Cu_3O_{6+y}$ (YBCO) are the best experimentally studied compounds in the low-doping regime. This is why the present work addresses these compounds. In LSCO the doping level of CuO_2 planes p practically coincides with Sr concentration, $p \approx x$, while in YBCO, because of the partial filling of oxygen chains, the doping level is different from the oxygen concentration y. In LSCO doping gives way to superconductivity at $p > p_{sc} \approx 0.055$ and in YBCO at $p > p_{sc} \approx 0.065$, see Fig. 1. At first sight this indicates full similarity. However, I will argue that the mechanisms behind p_{sc} in those two compounds are different and the closeness of the two values of p_{sc} is purely accidental. An important observation is that the normal-state electrical resistivities at $p < p_{sc}$ are very much different. At low temperature, $T \lesssim 100$ K, and at doping below the superconductivity threshold, the in-plane resistivity of LSCO exhibits[1,2] the Mott variable-range hopping regime $\rho \propto \exp\{(T_0/T)^{1/3}\}$. This indicates strong localization of holes in the Néel and the spin-glass regions of the LSCO phase diagram. These are the regions 1a and 1b in Fig. 1. On the other hand, the in-plane resistivity in YBCO at $p < p_{sc}$ shows only logarithmic dependence on temperature, $\rho \propto \ln(C/T)$, indicating weak-localization regime.[3,4] This is region 1 on the YBCO phase diagram, Fig. 1. For example, at $p \approx 0.04$ the in-plane resistivity of LSCO is about five times larger than that of YBCO at $T = 10$ K, and the same ratio is about 1000 at $T = 1$ K. Thus, role of disorder in LSCO below the superconductivity threshold is crucial while in YBCO the disorder is a relatively minor issue.

The magnetic properties of the compounds are also very much different. The three-dimensional antiferromagnetic (AF) Néel order in LSCO disappears at doping $p \approx 0.02$ and gives way to the so-called spin-glass phase. The incommensurate magnetic order has been observed at low temperature in neutron scattering. This order manifests itself as a scattering peak shifted with respect to the AF position. The incommensurate scattering has been observed even in the Néel phase where it coexists with the commensurate one. In the Néel phase, the incommensurability is almost doping independent and directed along the orthorhombic b axis.[5] In the spin-glass phase, the shift is directed along the b axis, and scales linearly with doping.[6] In the underdoped superconducting region ($0.055 \lesssim p \lesssim 0.12$), the shift still scales linearly with doping but it is directed along one of the crystal axes of the tetragonal lattice.[7] In YBCO the commensurate three-dimensional AF order exists up to $p \approx 0.065$, see Fig. 1. Moreover, there are indications that there is a narrow window around this doping where superconductivity and the commensurate AF order coexist.[8] Recently the incommensurate quasistatic spin ordering along the tetragonal a^* direction has been observed within the superconducting phase of YBCO (Refs. 9 and 10) at doping $p \approx 0.085$. The ordering becomes fully dynamic above $p \approx 0.1$.[11] Last, but not least, the observed incommensurate wave vector in YBCO at p

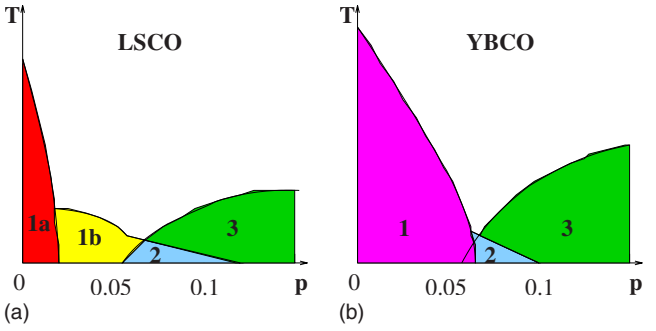

FIG. 1. (Color online) Schematic low-doping and low-temperature phase diagrams of LSCO and YBCO. LSCO: (1a) AF order coexists with diagonal incommensurate spin structure and strong localization of holes. (1b) Diagonal incommensurate spin structure and strong localization of holes. (2) Parallel incommensurate quasistatic spin structure and superconductivity. (3) Parallel incommensurate dynamic spin structure and superconductivity. YBCO: (1) AF order and weak localization of holes. (2) Parallel incommensurate quasistatic spin structure and superconductivity. (3) Parallel incommensurate dynamic spin structure and superconductivity.

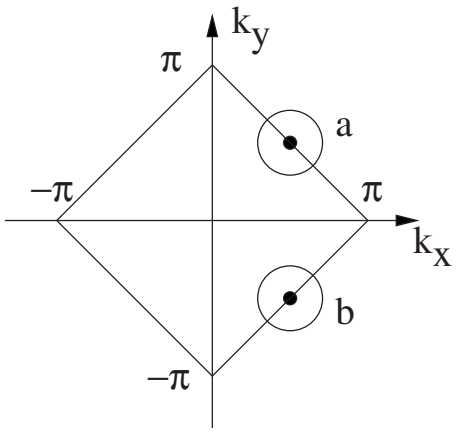

FIG. 2. Dispersion of a single hole in a Mott insulator is similar to that in a two-valley semiconductor.

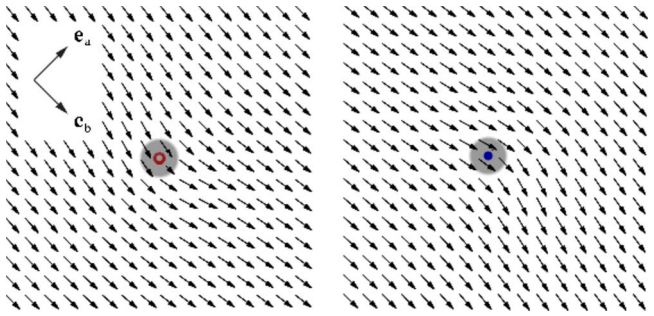

FIG. 3. (Color online) Distortion of the staggered spin fabric (small arrows) by the Sr-hole bound state. The left picture corresponds to the pseudospin directed out of the page and the right picture corresponds to the pseudospin directed in the page. Shaded area corresponds to the hole localization region. At large distances spins are directed along the orthorhombic b axis.

≈ 0.085 (Refs. 9 and 10) is of a factor of two smaller than the incommensurate wave vector in LSCO at the same doping.[7] On the other hand, at $p \approx 0.12$ the incommensurate wave vectors in LSCO and YBCO are equal.[7,11]

The phase diagram of underdoped LSCO has been explained in Refs. 12–14. The generic physics is based on the spin spirals. On the other hand a number of particular details of the LSCO phase diagram are driven by disorder. In YBCO, according to data on conductivity, the role of disorder is practically insignificant. This is quite natural since the doping mechanism in YBCO is different from that in LSCO. Therefore, having the same generic physics both compounds have different phase diagrams. The purpose of the present work is to explain the phase diagram of YBCO. In particular the following two most important issues are addressed. (1) Why does the AF order survive in YBCO up to a very large hole concentration $p \approx 0.06-0.07$? (2) Why is the pitch of the incommensurate spin order in YBCO different from that in LSCO? It will be demonstrated that both these issues are closely related and they are due to interlayer hopping in YBCO.

II. DISORDERED SPIN SPIRAL IN LSCO, $x < 0.055$

To understand differences and similarities between LSCO and YBCO, and hence to separate generic physics from material specific details, it is appropriate to summarize here briefly ideas of the approach[12–14] to LSCO. Dispersion of a single hole injected in a Mott insulator has minima at points $(\pm\pi/2, \pm\pi/2)$ as it is shown in Fig. 2. It is similar to the dispersion in a two-valley semiconductor. At low temperature, $T \lesssim 100$ K, and at doping $p < 0.055$ each hole is trapped in a hydrogenlike bound state near the corresponding Sr ion. The bound state can be built both with a hole from the a valley and with a hole from the b valley. Position of the Sr ion is above center of the Cu plaquette. Therefore energy of a hole residing on sublattice with spin up is the same as energy of a hole on sublattice down. Thus, in a perfect square lattice the "hydrogen" ground state is fourfold degenerate, two valley $\times$ two sublattice. In the real LSCO there is a small orthorhombic distortion of the lattice. Hence the valley degeneracy is lifted and the b valley has lower energy.[13,15] The sublattice degeneracy creates a frustration and hence a possibility to mix the hole states on different sublattices. It is convenient to describe the mixing using notion of pseudospin. The pseudospin is 1/2 since there are two sublattices. Solution of the single hole bound-state problem[12] demonstrates that the spin fabric is distorted in a local spiral shown in Fig. 3. Staggered spins are shown in accordance with notations of the σ model. The static spin distortion is always perpendicular to the pseudospin and decays $\propto 1/r$ at large distances. The local spin spiral is directed along the nodal direction corresponding to the valley of the hole, the b direction in Fig. 3. A finite concentration of Sr-hole bound states gives a ground state shown in Fig. 4. A particular random realization of Sr positions with concentration $x=0.05$ is presented. In Fig. 4 the $\vec{n}$ field (small arrows) representing staggered Cu spins is arbitrarily put in the ab plane. This is done to have the planar picture of the state. However, it is important to stress that without account for the Dzyaloshinski-Moriya and the XY anisotropies the plane of the coplanar spin configuration can be arbitrary. Recent neutron-scattering data at $x=0.05$ indicate that the static spins are in the bc plane.[17]

Fourier transform of the spin distribution shown in Fig. 4 gives the static spin structure factor

$$S_{\mathbf{q}} \propto \sum_{i,j} e^{i\mathbf{q}\cdot(\mathbf{r}_i-\mathbf{r}_j)} n^{\alpha}(\mathbf{r}_i) n^{\beta}(\mathbf{r}_j). \quad (1)$$

The calculated static spin structure factor on a sample with doping $x=0.04$ is shown in Fig. 5 together with experimental data taken by Fujita *et al.*[6]

Thus, the state of LSCO at $0.02 < p < 0.055$ is not a simple spin glass, it is a disordered spin spiral. Both the lower and the upper boundaries of this region are determined by the size of the bound state. The upper boundary, $p=0.055$, is a percolation point of isolated bound states. After the percolation the superconductivity becomes possible, and simultaneously direction of the spin spiral must rotate by 45°. The rotation is driven by the Pauli principle. To understand the mechanism of the rotation it is instructive to look at Fig. 6. Below the percolation point every hole is trapped in a

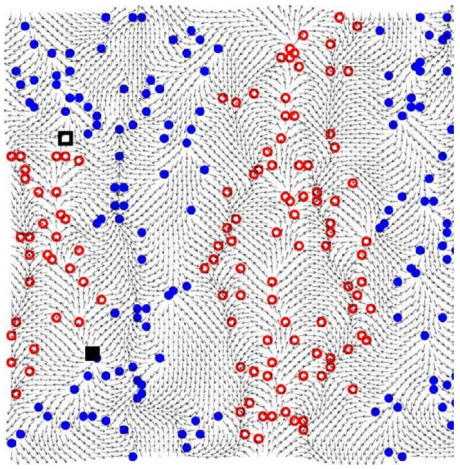

FIG. 4. (Color online) Disordered spin spiral: characteristic ground-state configuration of a particular realization of Sr positions at $x=0.05$. The horizontal direction coincides with the orthorhombic b axis and the vertical direction coincides with the orthorhombic a axis. The bound states pseudospins are oriented perpendicular to the plane of spins (in this case the plane of the picture). Open circles correspond to pseudospin direction out of the plane while full circles correspond to pseudospin direction into the plane. Small arrows represent staggered spins. The system forms domains stretched along the orthorhombic a direction, in which all the pseudospins are aligned in parallel.

bound state near its Sr ion. Wave functions of different holes do not overlap and hence the Pauli principle is not important. In this situation all the bound states reside in the b valley since, due to the orthorhombic deformation, the b valley is slightly lower than the a valley.[13,15] The population is shown in left of Fig. 6. Because of the population the wave vector of the spin spiral is directed along the b direction. After the percolation, $p>0.055$, holes are delocalized in space and hence the Pauli principle is important. The system reduces the Fermi motion kinetic energy by splitting holes between the pockets, as it is shown in right of Fig. 6. Holes in the a pocket "want" the spin-spiral wave vector along the a diagonal and holes in the b pocket want the spin-spiral wave

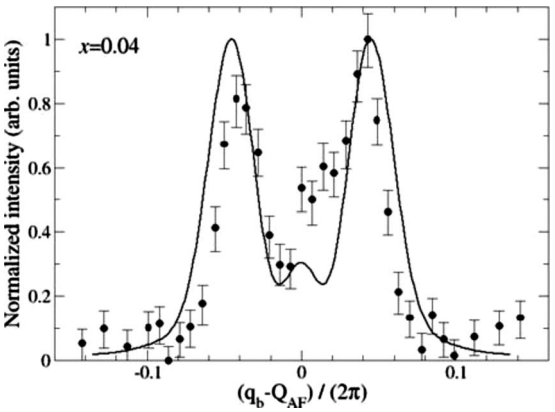

FIG. 5. Neutron scattering probability $S_{\mathbf{q}}$ for $x=0.04$. Full circles correspond to experimental observations taken from Fig. 4 in Ref. 6, with normalized intensities. The curve represents our simulation, containing no fitting parameters.

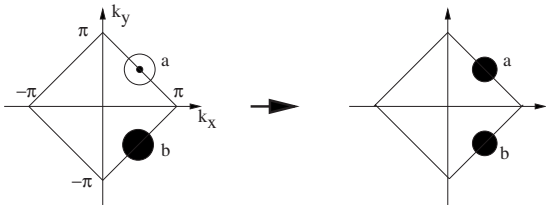

FIG. 6. Redistribution of holes in LSCO at the percolation point. The left picture corresponds to the localized regime, $p<0.055$, where holes reside in the b valley. The right picture corresponds to the delocalized regime, $p>0.055$, where holes split 50/50 between the a and b valleys.

vector along the b diagonal. The compromise is (1,0) or (0,1) direction. This explains the rotation of the spin-spiral direction *exactly* at the percolation point. Simultaneously the percolation gives a way to superconductivity.

The role of disorder in LSCO at $p>0.055$ is only marginal. Here the spin-spiral state suggested by Shraiman and Siggia[16] is realized. Most importantly, the state is superconducting and the spin spiral becomes dynamic at $p>0.11$.[18]

III. LSCO AT $x>0.055$. THE SPIN SPIRAL IN UNIFORMLY DOPED SINGLE CuO_2 LAYER

In this section we disregard the disorder. The analysis of the single CuO_2 layer with or without disorder is based on the two-dimensional t-t'-t''-J model at small doping. After integrating out the high energy fluctuations one comes to the effective low-energy action of the model.[18] Importantly, the integration of the high energy fluctuations is a fully controlled procedure; the small parameter justifying the procedure is the doping level, $p\ll 1$. The effective low-energy Lagrangian is written in terms of the bosonic $\vec{n}$ field ($n^2=1$) that describes the staggered component of the copper spins, and in terms of fermionic holons ψ. I use the term "holon" instead of "hole" because spin and charge are to large extent separated, see Ref. 18. The holon has a pseudospin that originates from two sublattices so the fermionic field ψ is a spinor acting on pseudospin. Minimums of the holon dispersion are at the nodal points $\mathbf{q}_0=(\pm\pi/2,\pm\pi/2)$. So, there are holons of two types (=two flavors) corresponding to two pockets. The dispersion in a pocket is somewhat anisotropic but for simplicity let us use here the isotropic approximation, $\epsilon(\mathbf{p})\approx\frac{1}{2}\beta\mathbf{p}^2$, where $\mathbf{p}=\mathbf{q}-\mathbf{q}_0$. The lattice spacing is set to be equal to unity, 3.81 Å$\rightarrow$1. All in all, the effective Lagrangian reads[18]

$$\mathcal{L}=\frac{\chi_\perp}{2}\dot{\vec{n}}^2-\frac{\rho_s}{2}(\nabla\vec{n})^2+\sum_\alpha\left\{\frac{i}{2}[\psi_\alpha^\dagger\mathcal{D}_t\psi_\alpha-(\mathcal{D}_t\psi_\alpha)^\dagger\psi_\alpha]\right.$$
$$\left.-\psi_\alpha^\dagger\epsilon(\mathcal{P})\psi_\alpha+\sqrt{2}g(\psi_\alpha^\dagger\vec{\sigma}\psi_\alpha)\cdot[\vec{n}\times(\boldsymbol{e}_\alpha\cdot\nabla)\vec{n}]\right\}. \quad (2)$$

The first two terms in the Lagrangian represent the usual nonlinear σ model. The magnetic susceptibility and the spin stiffness are $\chi_\perp\approx 0.53/8\approx 0.066$ and $\rho_s\approx 0.18$.[19] Hereafter the antiferromagnetic exchange in the initial t-J model is set to be equal to unity, $J\approx 130$ meV$\rightarrow$1. Note that ρ_s is the

bare spin stiffness; therefore by definition it is independent of doping. The rest of the Lagrangian in Eq. (2) represents the fermionic holon field and its interaction with the $\vec{n}$ field. The index $\alpha=a,b$ (flavor) indicates the pocket in which the holon resides. The pseudospin operator is $\frac{1}{2}\vec{\sigma}$, and $\mathbf{e}_\alpha=(1/\sqrt{2},\pm 1/\sqrt{2})$ is a unit vector orthogonal to the face of the magnetic Brillouin zone , where the holon is located. A very important point is that the argument of ϵ_α in Eq. (2) is a "long" (covariant) momentum,

$$\mathcal{P}=-i\nabla+\frac{1}{2}\vec{\sigma}\cdot[\vec{n}\times\nabla\vec{n}].$$

An even more important point is that the time derivatives that stay in the kinetic energy of the fermionic field are also long (covariant),

$$\mathcal{D}_t=\partial_t+\frac{i}{2}\vec{\sigma}\cdot[\vec{n}\times\dot{\vec{n}}].$$

An effective Lagrangian similar to Eq. (2) was suggested long time ago by Shraiman and Siggia.[16] However important covariant time derivatives were missing in their approach. The simplified version[16] is sufficient for semiclassical analysis of the system. However, the full version (2) is crucial for the excitation spectrum, quantum fluctuations, and especially for stability of the semiclassical solution with respect to quantum fluctuations. It is worth noting that the covariant derivatives in Eq. (2) are a reflection of the gauge invariance of the initial t-t'-t''-J model. Another important note is that effective Lagrangian (2) is valid regardless of whether the $\vec{n}$ field is static or dynamic. In other words, it does not matter if the ground-state expectation value of the staggered field is nonzero, $\langle\vec{n}\rangle\neq 0$, or zero, $\langle\vec{n}\rangle=0$. The only condition for validity of Eq. (2) is that all dynamic fluctuations of the $\vec{n}$ field are sufficiently slow. The typical energy of the $\vec{n}$-field dynamic fluctuations is $E_{\text{cross}}\propto p^{3/2}$, see Ref. 18, and it must be small compared to the holon Fermi energy $\epsilon_F\propto p$. The inequality $E_{\text{cross}}\ll\epsilon_F$ is valid up to optimal doping, $p\approx 0.15$. So, this is the regime where Eq. (2) is parametrically justified.

Numerical calculations within the t-t'-t''-J model with physical values of hopping matrix elements give the following values of the coupling constant and the inverse mass, $g\approx 1$, $\beta\approx 2.2$. Note that β is the inverse mass of the holon and the value $\beta=2.2$ corresponds to the effective mass

$$m^*=1.8m_e. \tag{3}$$

To describe LSCO at the very low doping, $p<0.055$, one needs to add to Eq. (2) a disordered random potential produced by Sr ions. The potential leads to the strong localization of holes as it is described in the previous section. The strong localization greatly simplifies the problem because charge degrees of freedom are frozen. Therefore the solution described in the previous section is not sensitive to the fine theoretical details such as covariant derivatives in Eq. (2). In other words the gauge invariance is not an important issue in the strongly localized regime.

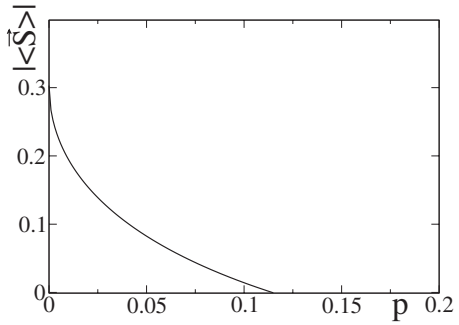

FIG. 7. The static component of spin versus doping at zero temperature. The point $p=0$ corresponds to the pure Heisenberg model where $\langle\vec{S}\rangle=0.303$.

The uniformly doped regime which is relevant to LSCO at $p>0.055$ is much more complicated. It requires the full scale theory. The dimensionless parameter,

$$\lambda=\frac{2g^2}{\pi\beta\rho_s}, \tag{4}$$

plays the defining role in the theory.[18] If $\lambda\leq 1$, the ground state corresponding to Lagrangian (2) is the usual Néel state and it stays collinear at any small doping. If $1\leq\lambda\leq 2$, the Néel state is unstable at arbitrarily small doping and the ground state is a static or dynamic spin spiral. The pitch of the spiral is

$$Q=\frac{g}{\rho_s}p. \tag{5}$$

If $\lambda\geq 2$, the system is unstable with respect to phase separation and/or charge-density-wave formation, and hence the effective long-wavelength Lagrangian (2) becomes meaningless. By the way, the pure t-J model ($t'=t''=0$) is unstable since it corresponds to $\lambda>2$.

To find experimental value of the coupling constant g it is sufficient to compare Eq. (5) with the pitch of the observed incommensurate spin structure at $0.055<p<0.12$. This gives $g\approx 1$ in a very good agreement with the prediction of the t-t'-t''-J model. Analysis of neutron inelastic-scattering data performed in Ref. 18 gives the value of inverse mass, $\beta\approx 2.7$. This also agrees reasonably well with the prediction of the t-t'-t''-J model. Using values of g and β found from fit of experimental data, one obtains that for LSCO

$$\lambda\approx 1.30. \tag{6}$$

Whether the spin spiral is static or dynamic depends on the doping level. Calculations[18] for uniformly doped single-layer t-t'-t''-J model with parameters corresponding to LSCO show that the static component of spin $\vec{S}$ vanishes at $p\approx 0.11$ as it is shown in Fig. 7. This is a quantum critical point. At the higher doping the spin spiral is purely dynamic. As it has been already pointed out one can compare Fig. 7 with data on LSCO only at $0.055<p<0.12$ where role of disorder in the real material is only marginal. At the lower doping the theory described in Sec. II is relevant.

IV. DOUBLE LAYER SPIN SPIRAL IN YBCO

The picture described in Secs. II and III, and based on the spin spirals explains qualitatively and quantitatively details of the underdoped LSCO phase diagram. To confirm the generic physics based on the spin spirals, one needs to explain also the phase diagram of underdoped YBCO. How is the described above physics changed in case of YBCO? It is well known that while LSCO contains a single CuO_2 layer per elementary cell YBCO contains two CuO_2 layers. Due to the bilayer structure the magnon spectrum in YBCO is split into acoustic and optic modes.[20] The optical gap is about 70 meV. This is substantially smaller than the maximum magnon energy $\sim 2J \sim 260$ meV. Therefore, the bilayer structure cannot substantially influence values of the effective coupling constant g and the inverse mass β which are due to magnetic fluctuations with the typical energy scale $\sim 2J$. So, one should expect that values of these parameters in YBCO are close to that in LSCO. The holon dispersion in YBCO is split into bilayer bonding and antibonding branches

$$\epsilon_{b,a} = \pm \frac{\Delta}{2} + \beta \frac{\boldsymbol{p}^2}{2}. \tag{7}$$

It is worth noting that for a perfect square lattice value of the nodal splitting Δ must be equal to zero, see discussion in Ref. 21. On the other hand both the Local-Density Approximation (LDA) calculation[21] and the Angle Resolved Photoemission Spectroscopy (ARPES) measurements[22] indicate a nonzero band splitting $\Delta \sim 100$ meV at nodal points. Most likely the splitting is due to the hole hopping via the interlayer oxygen chain sites.[23] The splitting Δ brings additional nontrivial physics in the system. In the present work Δ is used as a fitting parameter.

Let us impose the coplanar spiral configuration on the system

$$\vec{n}_1 = (\cos \mathbf{q} \cdot \mathbf{r},\ \sin \mathbf{q} \cdot \mathbf{r},\ 0),$$

$$\vec{n}_2 = -(\cos \mathbf{q} \cdot \mathbf{r},\ \sin \mathbf{q} \cdot \mathbf{r},\ 0), \tag{8}$$

where $\mathbf{q}$ is directed along the CuO bond [$\mathbf{q} \propto (1,0)$ or $\mathbf{q} \propto (0,1)$]. Here $\vec{n}_1$ and $\vec{n}_2$ correspond to the two layers. Note that $\vec{n}_1$ and $\vec{n}_2$ remain antiparallel at any given point $\mathbf{r}$; hence there is no admixture of the optic magnon to the ground-state configuration. In the spiral background [Eq. (8)] the single holon energy spectrum is of the form

$$\epsilon(\boldsymbol{p}) = \pm gq \pm \frac{\Delta}{2} + \beta \frac{\boldsymbol{p}^2}{2}, \tag{9}$$

where the first term is the spiral splitting caused by the $\sqrt{2} g \vec{\sigma} \cdot [\vec{n} \times (\boldsymbol{e}_\alpha \cdot \boldsymbol{\nabla}) \vec{n}]$ interaction in Eq. (2), the second term is the bonding-antibonding splitting, and the third term is the usual kinetic energy. The four branches of dispersion (9) are shown schematically in Fig. 8. Populations of the four bands depend on the doping level p and on the spiral wave vector q. To find the equilibrium value of q one needs to calculate the ground-state energy at a given doping p and pitch q, and then find minimum of the energy with respect to q. In the leading doping approximation only three terms from Eq. (2) contribute to the ground-state energy: the spin-elastic term

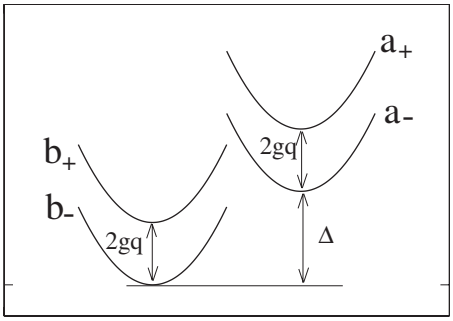

FIG. 8. Schematic dispersion of a holon. b and a corresponds to bonding and antibonding branches, and $\pm$ corresponds to the spiral splitting.

proportional to the spin stiffness ρ_s, the "spiral term" $\sqrt{2} g \vec{\sigma} \cdot [\vec{n} \times (\boldsymbol{e}_\alpha \cdot \boldsymbol{\nabla}) \vec{n}]$, and finally the Fermi motion energy.

When calculating energy, one has to remember that there are two CuO_2 planes in the unit cell. Therefore, the spin-elastic energy per unit area is $2 \times \rho_s q^2/2$, and the hole density per unit area is $2p$. It is convenient to define the following characteristic concentration

$$p_0 = \frac{\Delta}{\pi \beta}. \tag{10}$$

A straightforward calculation shows that there are three distinct regimes dependent on the doping:

$$(1) \quad p_0/2 > p > 0,$$

$$(2) \quad p_0 > p > p_0/2,$$

$$(3) \quad p > p_0.$$

In the first doping regime the antibonding a bands (see Fig. 8) are always empty. Hereafter only filled bands are mentioned. Both bonding b bands are filled at $q < \frac{\pi\beta}{g} p$ while at $q > \frac{\pi\beta}{g} p$ only the band b_- is filled. In the first regime ($p_0/2 > p > 0$) the energy is

$$\frac{E}{\rho_s} = \begin{cases} \left(1 - \frac{\lambda}{2}\right) q^2 + \frac{\pi\beta}{\rho_s} p^2, & q < \frac{\pi\beta}{g} p \\ q^2 - 2p \frac{g}{\rho_s} q + 2 \frac{\pi\beta}{\rho_s} p^2, & q > \frac{\pi\beta}{g} p \end{cases}.$$

It is convenient to introduce the following three wave vectors:

$$q_1 = \frac{\pi\beta}{g}(p_0 - p),$$

$$q_2 = \frac{\pi\beta}{g}\left(\frac{p_0}{4} + \frac{p}{2}\right),$$

$$q_3 = \frac{\pi\beta}{g}\left(\frac{p}{2} - \frac{p_0}{2}\right).$$

In the second doping regime, $p_0/2 < p < p_0$, the bonding bands $b_\pm$ are filled at $q < q_1$, the bands $b_\pm$ and a_- are filled at

$q_1 < q < q_2$, and b_- and a_- are filled at $q > q_2$. The energy in this regime reads

$$\frac{E}{\rho_s} = \begin{cases} \left(1 - \frac{\lambda}{2}\right) q^2 + \frac{\pi\beta}{\rho_s} p^2, & q < q_1 \\ \left(1 - \frac{2}{3}\lambda\right) q^2 + \frac{\lambda}{3} q q_1 - \frac{\lambda}{6} q_1^2 + \frac{\pi\beta}{\rho_s} p^2, & q_2 > q > q_1 \\ q^2 - 2p\frac{g}{\rho_s} q + \frac{\pi\beta}{\rho_s}\left(p^2 + pp_0 - \frac{p_0^2}{4}\right), & q > q_2 \end{cases} .$$

In the third doping regime, $p > p_0$, the bands $b_\pm$ and $a_\pm$ are filled at $q < q_3$, the bands $b_\pm$ and a_- are filled at $q_3 < q < q_2$, and b_- and a_- are filled at $q > q_2$. The energy in this case reads

$$\frac{E}{\rho_s} = \begin{cases} (1-\lambda) q^2 + \frac{\pi\beta}{\rho_s}\left(\frac{p^2}{2} - \frac{p_0^2}{2} + pp_0\right), & q < q_3 \\ \left(1 - \frac{2}{3}\lambda\right) q^2 - \frac{2\lambda}{3} q q_3 - \frac{2\lambda}{3} q_3^2 + \frac{\pi\beta}{\rho_s} p^2, & q_2 > q > q_3 \\ q^2 - 2p\frac{g}{\rho_s} q + \frac{\pi\beta}{\rho_s}\left(p^2 + pp_0 - \frac{p_0^2}{4}\right), & q > q_2 \end{cases} .$$

The minimum of the energy with respect to q gives the equilibrium spiral pitch Q at a given doping level p. The minimization shows that the value of Q depends on λ. For $1 < \lambda < \frac{3}{2}$ the pitch stays zero for $p < p_0$, then for $p_0 < p < p_1$, where $p_1 = 0.5p_0/(\lambda - 1)$, the pitch is

$$Q = \frac{g}{\rho_s} \frac{p - p_0}{3 - 2\lambda}, \tag{11}$$

and finally at $p > p_1$ the pitch is given by single-layer formula (5). This behavior is illustrated in Fig. 9 (left).

In the case $\frac{3}{2} < \lambda < 2$ the spin-spiral pitch stays zero until the critical concentration $p_c = \frac{1}{\lambda}(1 + \sqrt{1 - \frac{\lambda}{2}})p_0$, and then it jumps to single-layer value (5), see Fig. 9 (right). I would like to reiterate once more that the considered picture is valid for both the static and the dynamic spirals. Ultimately, the spiral always becomes dynamic at $p \geq 0.1 - 0.12$, see Ref. 18.

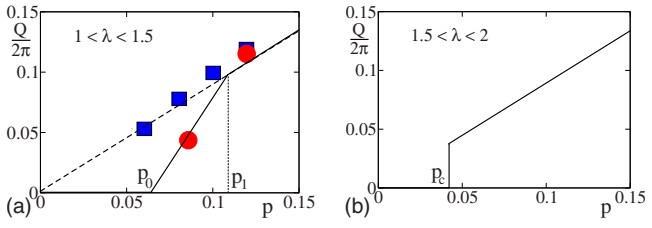

FIG. 9. (Color online) Incommensurate pitch of the spin spiral versus doping. Left: the regime $1 < \lambda < 1.5$. The solid line is the theory prediction for YBCO, and the parameters are $\lambda = 1.3$ and $p_0 = 0.065$. The dashed line is the theory prediction for LSCO. Note that the theory has no adjustable parameters relevant to the data presented in this figure. The red circles represent the YBCO neutron-scattering data from Refs. 9–11. The blue squares represent the LSCO neutron-scattering data from Ref. 7. Right: theoretical prediction for the pitch in the double-layer case for $1.5 < \lambda < 2$.

Clearly at $\frac{3}{2} < \lambda < 2$ the jump at $p = p_c$ is the first-order phase transition. On the other hand, p_0 and p_1 at $1 < \lambda < \frac{3}{2}$ are Lifshitz points.

V. COMPARISON WITH EXPERIMENT

The value of coupling g predicted by the t-t'-t''-J model is $g \approx 1.0$; this is a very robust prediction, see Refs. 12 and 13. The value of the Heisenberg model spin stiffness, $\rho_s \approx 0.18$, is known very well;[19] it is also robust. The value of the effective mass predicted by the t-t'-t''-J model is $m^* \approx 1.8m_e$, see Eq. (3). The effective-mass prediction is not robust; the mass value is sensitive to t, t', t'', and to some other details. With the values of parameters predicted by the t-t'-t''-J model the dimensionless parameter λ, see Eq. (4), is $\lambda \approx 1.5$. This value can be fine tuned using experimental data on inelastic neutron scattering from LSCO. The fine tuning[18] gives $\lambda \approx 1.3$. This value of λ corresponds to the effective mass of the holon $m^* = 1.5m_e$. The parameter λ cannot be influenced by the relatively weak interlayer coupling; therefore the same value should be used for YBCO as well as for all other cuprates.[24] According to Refs. 4 and 8 the AF order in YBCO extends up to $p = 0.06 - 0.07$ so we take $p_0 \approx 0.065$. This is the only adjustable parameter of the theory relevant specifically to YBCO. Having g, ρ_s, λ, and p_0 Eq. (11) predicts the incommensurate wave vector in YBCO. The prediction is shown in Fig. 9 (left) by the solid line. The theory agrees very well with neutron-scattering data shown by red circles.[9–11] Using Eq. (10) one finds the value of the bonding-antibonding splitting, $\Delta \approx 70$ meV. This is consistent with LDA calculations[21] and with ARPES data.[22] In the same Fig. 9 (left) the single-layer theoretical $Q(p)$, Eq. (5), is shown by the dashed line, and the neutron-scattering LSCO data[7] are shown by the blue squares. All in all the theory agrees with experimental data for both YBCO and LSCO

remarkably well. Note that theoretical curves presented in Fig. 9 (left) have no adjustable parameters relevant to the experimental data presented in the same figure. The only adjustable parameter of the YBCO theory, p_0, has been determined from different measurements.[4,8]

The developed theory is based on the small-p expansion. Therefore, it is not surprising that at $p>0.12$ the experimental data start to deviate from the theory. Note also that the single-layer formula (5) is not applicable to LSCO at $p<0.055$. The region $p<0.055$ in LSCO corresponds to the strong localization regime and the relevant theory was developed in Ref. 14.

VI. CONCLUSIONS

The incommensurate spin ordering properties and the phase diagrams of the single-layer LSCO and of the double-layer YBCO are very much different, see Fig. 1. Nevertheless the underlying generic physics is the same and the spin-spiral theory explains quantitatively both phase diagrams. The theory explains also the difference in the incommensurate pitches, see Fig. 9. Material specific details are driven by the intrinsic disorder in LSCO and by the bilayer structure in YBCO.

The present analysis allows making an observation that the superconductivity is intimately related to the incommensurate spin ordering. In LSCO this relation is masked by the intrinsic disorder; superconductivity is impossible in the strongly localized regime and therefore onset of superconductivity is determined by percolation. However, in YBCO the correlation between superconductivity and incommensurate spin ordering is clear; the critical concentration for onset of superconductivity practically coincides with that for onset of the incommensurate spin order.

ACKNOWLEDGMENTS

I am grateful to O. K. Andersen and V. Hinkov for important discussions.

[1] B. Keimer, A. Aharony, A. Auerbach, R. J. Birgeneau, A. Cassanho, Y. Endoh, R. W. Erwin, M. A. Kastner, and G. Shirane, Phys. Rev. B **45**, 7430 (1992); M. A. Kastner, R. J. Birgeneau, G. Shirane, and Y. Endoh, Rev. Mod. Phys. **70**, 897 (1998).

[2] Y. Ando, K. Segawa, S. Komiya, and A. N. Lavrov, Phys. Rev. Lett. **88**, 137005 (2002).

[3] X. F. Sun, K. Segawa, and Y. Ando, Phys. Rev. B **72**, 100502(R) (2005).

[4] N. Doiron-Leyraud, M. Sutherland, S. Y. Li, L. Taillefer, R. Liang, D. A. Bonn, and W. N. Hardy, Phys. Rev. Lett. **97**, 207001 (2006).

[5] M. Matsuda, M. Fujita, K. Yamada, R. J. Birgeneau, Y. Endoh, and G. Shirane, Phys. Rev. B **65**, 134515 (2002).

[6] M. Fujita, K. Yamada, H. Hiraka, P. M. Gehring, S. H. Lee, S. Wakimoto, and G. Shirane, Phys. Rev. B **65**, 064505 (2002).

[7] K. Yamada, C. H. Lee, K. Kurahashi, J. Wada, S. Wakimoto, S. Ueki, H. Kimura, Y. Endoh, S. Hosoya, G. Shirane, R. J. Birgeneau, M. Greven, M. A. Kastner, and Y. J. Kim, Phys. Rev. B **57**, 6165 (1998).

[8] R. I. Miller, R. F. Kiefl, J. H. Brewer, F. Callaghan, J. E. Sonier, R. Liang, D. A. Bonn, and W. Hardy, Phys. Rev. B **73**, 144509 (2006).

[9] V. Hinkov, P. Bourges, S. Pailhes, Y. Sidis, A. Ivanov, C. D. Frost, T. G. Perring, C. T. Lin, D. P. Chen, and B. Keimer, Nat. Phys. **3**, 780 (2007).

[10] V. Hinkov, D. Haug, B. Fauque, P. Bourges, Y. Sidis, A. Ivanov, C. Bernhard, C. T. Lin, and B. Keimer, Science **319**, 597 (2008).

[11] V. Hinkov, S. Pailhes, P. Bourges, Y. Sidis, A. Ivanov, A. Kulakov, C. T. Lin, D. P. Chen, C. Bernhard, and B. Keimer, Nature (London) **430**, 650 (2004).

[12] O. P. Sushkov and V. N. Kotov, Phys. Rev. Lett. **94**, 097005 (2005).

[13] A. Lüscher, G. Misguich, A. I. Milstein, and O. P. Sushkov, Phys. Rev. B **73**, 085122 (2006).

[14] A. Lüscher, A. I. Milstein, and O. P. Sushkov, Phys. Rev. Lett. **98**, 037001 (2007).

[15] O. P. Sushkov, Wenhui Xie, O. Jepsen, O. K. Andersen, and G. A. Sawatzky, Phys. Rev. B **77**, 035124 (2008).

[16] B. I. Shraiman and E. D. Siggia, Phys. Rev. Lett. **61**, 467 (1988); **62**, 1564 (1989); Phys. Rev. B **42**, 2485 (1990).

[17] M. Matsuda (private communication).

[18] A. I. Milstein and O. P. Sushkov, Phys. Rev. B **78**, 014501 (2008).

[19] R. R. P. Singh, Phys. Rev. B **39**, 9760 (1989); Zheng Weihong, J. Oitmaa, and C. J. Hamer, *ibid.* **43**, 8321 (1991).

[20] D. Reznik, P. Bourges, H. F. Fong, L. P. Regnault, J. Bossy, C. Vettier, D. L. Milius, I. A. Aksay, and B. Keimer, Phys. Rev. B **53**, R14741 (1996); S. M. Hayden, G. Aeppli, T. G. Perring, H. A. Mook, and F. Dogan, *ibid.* **54**, R6905 (1996).

[21] O. K. Andersen, A. I. Liechtenstein, O. Jepsen, and F. Paulsen, J. Phys. Chem. Solids **56**, 1573 (1995).

[22] S. V. Borisenko, A. A. Kordyuk, V. Zabolotnyy, J. Geck, D. Inosov, A. Koitzsch, J. Fink, M. Knupfer, B. Buchner, V. Hinkov, C. T. Lin, B. Keimer, T. Wolf, S. G. Chiuzbaian, L. Patthey, and R. Follath, Phys. Rev. Lett. **96**, 117004 (2006).

[23] O. K. Andersen (private communication).

[24] The hopping matrix elements t' and t'' in YBCO are slightly different from that in LSCO. This can give a small difference in the value of λ.